

A CFL condition for the finite cell method

Tim Bürchner^{*1}, Lars Radtke² and Philipp Kopp³

¹Chair of Computational Modeling and Simulation, Technische Universität München

²Institute for Ship Structural Design and Analysis, Technische Universität Hamburg

³Chair of Data Science in Civil Engineering, Bauhaus-Universität Weimar

Abstract

Immersed boundary finite element methods allow the user to bypass the potentially troublesome task of boundary-conforming mesh generation. However, they suffer from the influence of cut elements, i.e., elements that are intersected by the physical domain boundaries. When combined with explicit time integration, poorly cut elements with little support in the physical domain have a detrimental effect on the critical time step size, thereby hampering the application of immersed boundary methods to wave propagation simulations. In this paper, we investigate the stabilizing effect of the finite cell method concerning explicit time integration. Starting with an analytical solution of an example with one degree of freedom, we systematically study the influence of α -stabilization on the maximum eigenvalue and thus on the critical time step size. The analysis is then complemented by a numerical study of an example with one element and an increasing polynomial degree. We demonstrate that the critical time step size does not decrease below a certain limit, even when further reducing the cut fraction of the element. This minimum critical time step size is controlled by the chosen α value and becomes less severe for higher dimensions. Increasing the polynomial degree has little effect on the degradation of the minimum critical time step size. Finally, we provide an estimate of the minimum critical time step size depending on the chosen stabilization parameter α and the dimension of the problem. Based on this estimate, we propose a modified CFL condition for the finite cell method, the validity of which we demonstrate on a numerical example of a perforated plate.

Keywords: wave equation, explicit dynamics, finite cell method, spectral element method, central difference method, CFL condition

1 Introduction

The efficient and accurate simulation of acoustic and elastic wave propagation is an essential task in many scientific disciplines, such as seismology [1, 2], medical imaging [3], structural health monitoring [4], or non-destructive testing [5]. While grid-point methods such as the finite difference method (FDM) approximate the underlying partial differential equation (PDE) on a discrete set of grid points, the finite element method (FEM) divides the spatial domain into elements and approximates the solution by a set of basis functions with corresponding coefficients that satisfy the weak form of the PDE [6]. Due to the simplicity of its basic formulation and its efficiency when combined with explicit time integration schemes, FDM and its variants enjoy great popularity in many applications. However, when confronted with complex geometries, the implementation of FDM and its boundary conditions becomes challenging [6]. Standard FEM accurately resolves arbitrary geometries with boundary-conforming meshes and allows to straightforwardly impose all kinds of boundary conditions, e.g., reflecting or absorbing boundaries. Higher-order approaches, such as the spectral element method (SEM) [7, 8], exploit the spectral convergence with respect to the functional interpolation of polynomials to reduce the discretization error. In wave propagation simulation, SEM is

^{*}tim.buerchner@tum.de, Corresponding author

widely used due to its favorable properties in terms of accuracy and efficiency [9]. A clever combination of the basis functions' interpolation points and the quadrature rule results in a diagonal mass matrix without deteriorating the solution quality. Integrating in time with explicit methods, such as the central difference method (CDM), then becomes trivial and leads to excellent parallel scaling properties and low memory requirements [10]. The corresponding critical time step size of the time integration can be determined with the CFL condition [11], which takes into account the wave speed and the element size, as well as the Courant number of the CDM, the spectral radius of SEM, and the dimension of the problem [9]. Despite – or rather because of – the underintegration of the mass matrix, SEM shows a p times higher accuracy than classical FEM, where p is the polynomial degree of the shape functions [12], as long as the element distortion is moderate [13]. In addition, the critical time step size increases as a consequence of nodal lumping, since eigenvalues are now approached from below in SEM, whereas they are approached from above in classical FEM.

Nevertheless, generating higher-order boundary-conforming hexahedral meshes remains a tedious task [6]. Immersed boundary methods (IBM) overcome this challenge by embedding the domain of interest in an extended domain with a simple shape. While the extended domain can be easily meshed with a non-boundary-conforming mesh (for example, a Cartesian grid), cut elements with little support in the physical domain have adverse effects on the conditioning of the mass and stiffness matrices and the critical time step size during explicit time integration [14, 15]. However, α -stabilization introduced by the finite cell method (FCM) [16, 17] imposes an upper limit on the conditioning of the matrices and a lower limit on the critical time step size, as we show later. De Prenter et al. [14] give a comprehensive overview of the conditioning and stability of IBMs and discuss possible remedies, focusing on non-dynamic problems. A variety of approaches exist to address the challenges of badly cut elements, such as FCM and its isogeometric version (IGA-FCM) [18], which is studied in [19, 20, 15]. Alternatives are cutFEM [21, 22], aggregated FEM [23, 24], cgFEM [25], or the shifted boundary method [26, 27]. Approaches specifically tailored to IBMs for explicit hyperbolic problems include eigenvalue stabilization (EVS) [28], local time stepping [29, 30], and implicit-explicit (IMEX) time integration [31–34]. While the above references primarily study the accuracy per degree of freedom, the work in [35] analyzes computation times for SCM and IGA-FCM, which also depend on the sparsity of the system matrices and the time integration scheme used.

However, to the authors' knowledge, the influence of the α -stabilization of FCM on the critical time step size has not been studied in detail. We therefore investigate this relationship by conducting analytical and numerical studies on the FCM-discretized scalar wave equation. For higher polynomial degrees, we consider FCM together with spectral basis functions, a combination that is often referred to as spectral cell method (SCM) [36, 37]. Lumping of cut elements is not used, as it has been shown to significantly degrade the accuracy of SCM simulations [32, 15, 33, 35]. We expect that some of our results obtained in this study translate to other stabilization approaches.

The remainder of the paper is organized as follows. Section 2 introduces the scalar wave equation and its spatial discretization with SCM. Section 3 analytically studies how α -stabilization affects the critical time step size on an example with a single linear finite element that is constrained to have only one degree of freedom for any dimension. Section 4 then numerically examines how these results translate to higher polynomial degrees again using one finite element. In Section 5, we propose an estimate of the minimum critical time step size and derive a modified CFL condition for the finite cell method. We verify our results on a two-dimensional perforated plate, where we vary the circle positions to cover as many cut configurations as possible. Finally, Section 6 summarizes the paper and outlines the implications for explicit dynamics with FCM in practice.

2 Scalar wave equation and finite cell method

Given a density ρ , a wave speed c , and a distributed load f , the second-order scalar wave equation for the scalar primary field Ψ is

$$\rho \ddot{\Psi} - \nabla \cdot (\rho c^2 \nabla \Psi) = \rho f \quad \text{in } \Omega \times [0, T], \quad (1)$$

where $\Omega \subset \mathbb{R}^d$ is the physical domain with the position vector $\mathbf{x} \in \mathbb{R}^d$ and spatial dimension d , and $T > 0$ is the final time. We explicitly include the density in (1) since the material interpretation of

the finite cell method for the scalar wave equation eliminates the influence of the fictitious domain by reducing the density there. We also define the Neumann and Dirichlet boundary conditions

$$\nabla \Psi \cdot \mathbf{n} = \bar{v}_n \quad \text{on } \Gamma^N, \quad \text{and} \quad \Psi = \bar{\Psi} \quad \text{on } \Gamma^D, \quad (2)$$

where \mathbf{n} is the outward-pointing unit normal vector and $\Gamma^N \cup \Gamma^D = \partial\Omega$, such that $\Gamma^N \cap \Gamma^D = \emptyset$. We finalize the problem definition by introducing the initial states $\Psi(\mathbf{x}, 0) = \Psi_0(\mathbf{x})$ and $\dot{\Psi}(\mathbf{x}, 0) = \dot{\Psi}_0(\mathbf{x})$.

Following the philosophy of immersed boundary finite element methods we embed the physical domain Ω in an extended domain Ω^e of simple shape, which can be easily meshed, e.g., with a Cartesian grid. The finite cell method then introduces the indicator function

$$\alpha^{\text{FCM}}(\mathbf{x}) = \begin{cases} 1 & \text{for } \mathbf{x} \in \Omega, \\ \alpha & \text{else,} \end{cases} \quad (3)$$

to distinguish between the physical domain Ω and fictitious domain $\Omega^f = \Omega^e \setminus \Omega$, where $\alpha \in [0, 1]$ is a stabilization parameter. Multiplying (1) by a test function $\delta\Psi$, integrating by parts, multiplying by α^{FCM} , and substituting the Neumann boundary condition results in the stabilized weak form of the scalar wave equation:

$$\int_{\Omega^e} \alpha^{\text{FCM}} \rho \ddot{\Psi} \delta\Psi + \alpha^{\text{FCM}} \rho c^2 \nabla \Psi \cdot \nabla \delta\Psi \, d\Omega^e = \int_{\Omega^e} \alpha^{\text{FCM}} \rho f \delta\Psi \, d\Omega^e + \int_{\Gamma^N} \alpha^{\text{FCM}} \rho c^2 \bar{v}_n \delta\Psi \, d\Gamma^N. \quad (4)$$

Choosing $\alpha = 0$ recovers the original solution in Ω , but also results in a loss of definiteness since there is no equation to determine Ψ inside Ω^f . Selecting a small value for α instead recovers definiteness and imposes upper limits to the condition numbers of the mass and stiffness matrices, and to the largest eigenvalue of the corresponding generalized eigenvalue problem [14]. This α -stabilization introduces a consistency error that scales with $\sqrt{\alpha}$ in the energy norm for Laplace and Helmholtz problems [38]. As outlined in [17], we can interpret α -stabilization from a continuum mechanics point of view as scaling the density of the material by α in the fictitious domain while leaving the wave speed untouched.

Applying the Bubnov-Galerkin method, we then use the same set of multivariate basis functions $\{N_i\}_{1 \leq i \leq n^{\text{dof}}}$ to define the approximation of Ψ and the test functions $\delta\Psi$, where n^{dof} is the total number of basis functions. Following standard finite element procedures, we construct N_i using tensor products of univariate Lagrange polynomials $N_i^{\text{Lag},p}$ of order p which we connect across adjacent elements. We define $N_i^{\text{Lag},p}$ to interpolate the Gauss-Lobatto-Legendre (GLL) points, which allows us to obtain diagonal mass matrices (nodal lumping) when also using the GLL points as a quadrature rule. Denoting $\xi_{0,k}^{\text{Lo},p-1}$, $k = 1, 2, \dots, p-1$ as the roots of Lobatto polynomials of order $p-1$, the $p+1$ GLL points on a reference interval $[-1, 1]$ are

$$\xi_j = \begin{cases} -1 & \text{if } j = 1 \\ \xi_{0,j-1}^{\text{Lo},p-1} & \text{if } 2 \leq j < p+1 \\ 1 & \text{if } j = p+1 \end{cases} \quad (5)$$

The univariate Lagrange polynomials then take the form

$$N_i^{\text{Lag},p}(\xi) = \prod_{j=1, j \neq i}^{p+1} \frac{\xi - \xi_j}{\xi_i - \xi_j} \quad \text{for } i = 1, 2, \dots, p+1. \quad (6)$$

By discretizing (4) in this way, we obtain a semi-discrete system of ordinary differential equations

$$\mathbf{M} \ddot{\Psi} + \mathbf{K} \Psi = \mathbf{F}, \quad (7)$$

where Ψ is the solution vector containing the unknown basis function coefficients, \mathbf{M} is the mass matrix, \mathbf{K} is the stiffness matrix, and \mathbf{F} is the right-hand side vector.

The time integration of (7) is commonly performed by the explicit CDM due to its simplicity. As detailed in the introduction, the critical time step size and, hence, the largest eigenvalue are

a major obstacle for combining most immersed boundary methods with explicit time integration schemes. This is because cut elements with little support in the physical domain lead to large eigenvalues, making stabilization methods inevitable. Let $\lambda_{\max}(\mathbf{K}, \mathbf{M})$ denote the largest eigenvalue of the generalized eigenvalue problem associated with the stiffness and mass matrices. Then, the critical time step size of the CDM [39] is given by

$$\Delta t_{\text{crit}} = \frac{2}{\sqrt{\lambda_{\max}(\mathbf{K}, \mathbf{M})}}. \quad (8)$$

3 Analytic investigations

Problem statement

We start with a single-element setup, which we reduce to a system with one degree of freedom for arbitrary dimensions by choosing linear shape functions and appropriate Dirichlet boundary conditions. Because of its simplicity, we can solve the problem analytically, which leads to insights into α -stabilization and the way it imposes a lower limit on the critical time step size, regardless of the severity of an element's cut. We consider a linear element where the physical domain is determined by a single cut parameter χ . Dirichlet boundary conditions are imposed such that the problem inherits only a single degree of freedom corresponding to a single linear basis function associated to the node opposite of the origin. Figure 1 illustrates the problem for the dimensions $d = 1, 2$, and 3.

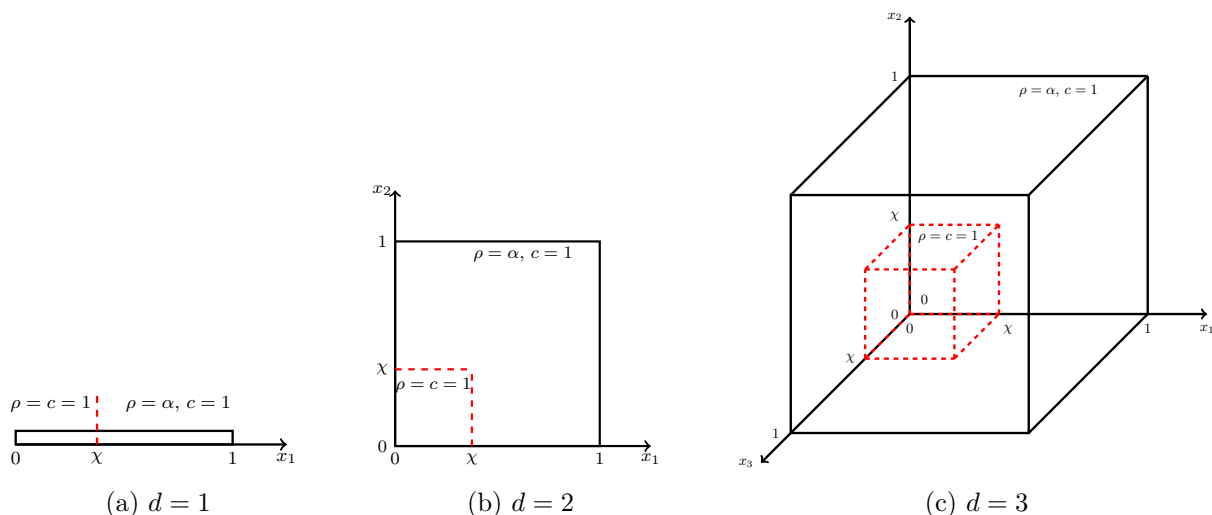


Figure 1: Investigated systems of increasing dimension. Dirichlet boundary conditions of the example with one degree of freedom corresponding to $x_1 = 0$ are marked in transparent blue, corresponding to $x_2 = 0$ in transparent green, and corresponding to $x_3 = 0$ in transparent yellow.

Regardless of the spatial dimension of the problem, we define uniform material parameters $\rho = c = 1$ in the physical domain. According to the interpretation of FCM as density scaling of the material, the density in the fictitious domain is $\rho = \alpha$, while the wave speed $c = 1$ remains unaffected. For the 1D case, the domain $\Omega^e = [0, 1]$ is divided into the physical domain $\Omega = [0, \chi]$ and the fictitious domain $\Omega^f = (\chi, 1]$. Imposing a Dirichlet boundary condition on the left side of the domain $\Psi(0) = 0$ leads to a system with only one degree of freedom belonging to the basis function $N(x) = x$.

This problem can be trivially generalized to any dimension. For an arbitrary dimension d , the extended domain is covered by a d -dimensional hypercube $\Omega^e = [0, 1]^d$ with edge length one. Correspondingly, the physical domain is captured by a d -dimensional hypercube $\Omega = [0, \chi]^d$ with edge length χ . As mentioned before, the fictitious domain is $\Omega^f = \Omega^e \setminus \Omega$. The imposed Dirichlet boundary conditions are $\Psi([x_1 \dots x_{i-1} \ x_i = 0 \ x_{i+1} \dots x_d], t) = 0$ for $i = 1, 2, \dots, d$. For 2D this corresponds to $\Psi([x_1 \ x_2], t) = \Psi([x_1 \ x_2 = 0], t) = 0$ and for 3D to $\Psi([x_1 \ x_2 \ x_3], t) = \Psi([x_1 \ x_2 = 0$

$x_3], t) = \Psi([x_1 \ x_2 \ x_3 = 0], t) = 0$. The available basis function $N(\mathbf{x})$ belonging to the only degree of freedom is

$$N(\mathbf{x}) = \prod_{i=1}^d x_i \quad (9)$$

where x_i , $i = 1, 2, \dots, d$, denote the components of the spatial position vector \mathbf{x} . In all cases, the volume fraction $\phi(c) = \frac{V(\Omega)}{V(\Omega^e)} = \chi^d \rightarrow 0$ tends to zero as the cut parameter $\chi \rightarrow 0$ goes to zero, where $V(\Omega)$ and $V(\Omega^e)$ denote the volumes of the physical and extended domains. For systems with one degree of freedom, the mass and stiffness matrices M and K are scalar. Depending on the cut χ and the stabilization parameter α , the scalar mass and stiffness are equal to

$$M = \int_{\Omega} N^2(\mathbf{x}) d\Omega + \int_{\Omega^f} \alpha N^2(\mathbf{x}) d\Omega^f = \int_{\Omega} (1 - \alpha) N^2(\mathbf{x}) d\Omega + \int_{\Omega^e} \alpha N^2(\mathbf{x}) d\Omega^e, \quad (10)$$

$$\begin{aligned} K &= \int_{\Omega} \nabla N(\mathbf{x}) \cdot \nabla N(\mathbf{x}) d\Omega + \int_{\Omega^f} \alpha \nabla N(\mathbf{x}) \cdot \nabla N(\mathbf{x}) d\Omega^f \\ &= \int_{\Omega} (1 - \alpha) \nabla N(\mathbf{x}) \cdot \nabla N(\mathbf{x}) d\Omega + \int_{\Omega^e} \alpha \nabla N(\mathbf{x}) \cdot \nabla N(\mathbf{x}) d\Omega^e. \end{aligned} \quad (11)$$

The eigenvalue of the system is obtained by dividing the stiffness by the mass $\lambda = \frac{K}{M}$.

Results

In 1D, the basis function is $N(x) = x$ and the gradient is $\nabla N(x) = 1$. We can express the mass and stiffness as a function of α and χ :

$$M(\chi, \alpha) = \int_0^\chi (1 - \alpha) x^2 dx + \int_0^1 \alpha x^2 dx = \frac{1}{3}((1 - \alpha)\chi^3 + \alpha), \quad (12)$$

$$K(\chi, \alpha) = \int_0^\chi (1 - \alpha) dx + \int_0^1 \alpha dx = (1 - \alpha)\chi + \alpha. \quad (13)$$

The system has one eigenvalue, which is

$$\lambda(\chi, \alpha) = \frac{K}{M} = 3 \frac{(1 - \alpha)\chi + \alpha}{(1 - \alpha)\chi^3 + \alpha}. \quad (14)$$

Figure 2 shows M and K depending on χ and α , when the cut parameter and stabilization are varied logarithmically between $\chi \in [10^{-16}, 10^0]$ and $\alpha \in [10^{-16}, 10^0]$, resulting in a logarithmically spaced grid of 801×801 points. Equivalently, the eigenvalue is shown on the left side of Figure 3, while the critical time step sizes with respect to the cut parameter χ for nine different α values are shown on the right side.

In 2D, the bivariate basis function is $N(x_1, x_2) = x_1 x_2$, and the corresponding gradient is $\nabla N = [x_2 \ x_1]$. For mass and stiffness, we can write

$$M(\chi, \alpha) = \int_0^\chi \int_0^\chi (1 - \alpha) x_1^2 x_2^2 dx_1 dx_2 + \int_0^1 \int_0^1 \alpha x_1^2 x_2^2 dx_1 dx_2 = \frac{1}{9}((1 - \alpha)\chi^6 + \alpha), \quad (15)$$

$$K(\chi, \alpha) = \int_0^\chi \int_0^\chi (1 - \alpha) (x_2^2 + x_1^2) dx_1 dx_2 + \int_0^1 \int_0^1 \alpha (x_2^2 + x_1^2) dx_1 dx_2 = \frac{2}{3}((1 - \alpha)\chi^4 + \alpha). \quad (16)$$

The eigenvalue is then

$$\lambda(\chi, \alpha) = 6 \frac{(1 - \alpha)\chi^4 + \alpha}{(1 - \alpha)\chi^6 + \alpha}. \quad (17)$$

Equivalent to the 1D example, Figure 4 illustrates the eigenvalue of the 2D problem on the left side and the critical time step size for nine different α values on the right side.

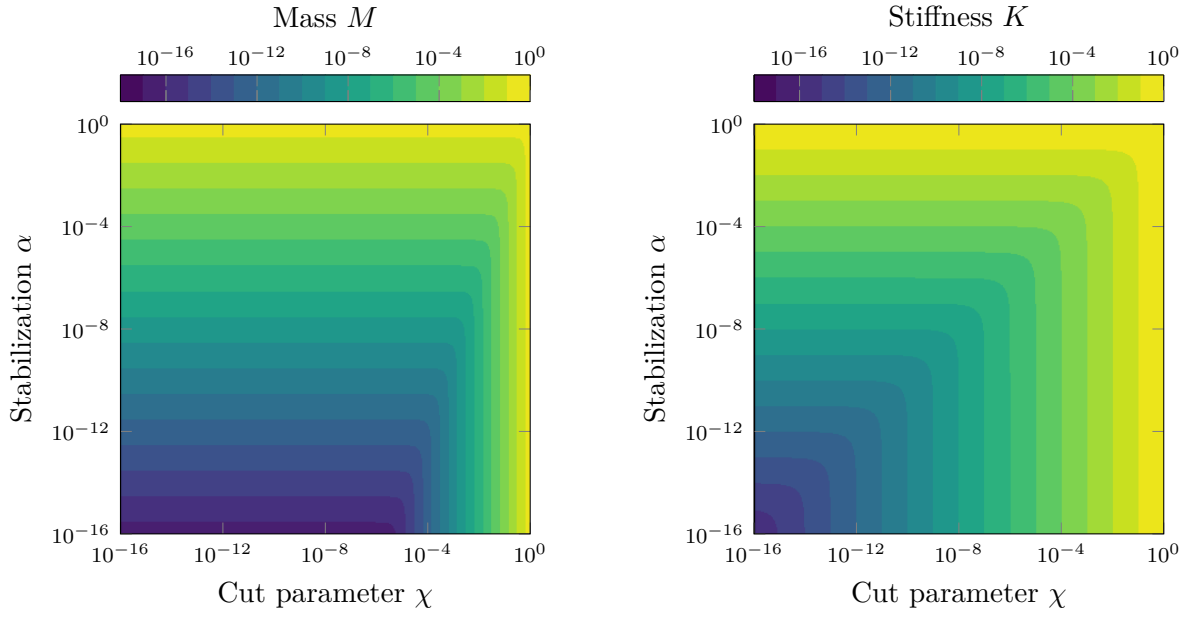


Figure 2: Scalar mass M (left) and stiffness K (right) of the one-dimensional system with one degree of freedom.

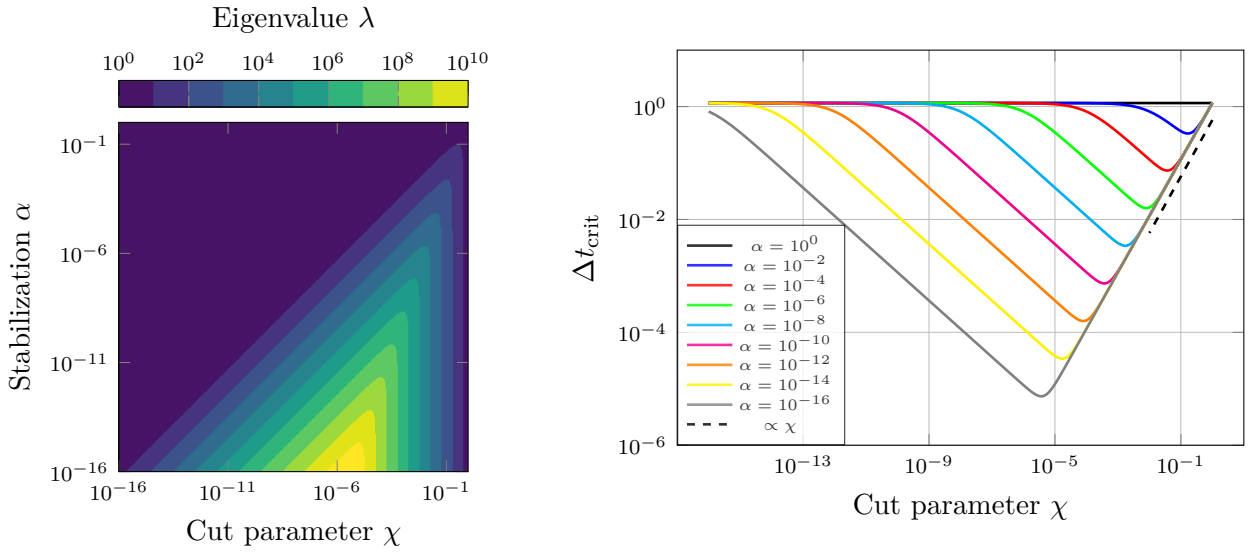


Figure 3: Eigenvalue λ (left) and corresponding critical time step size Δt_{crit} (right) of the one-dimensional system with one degree of freedom.

In 3D, the trivariate basis function is $N(x_1, x_2, x_3) = x_1 x_2 x_3$, and the corresponding gradient is

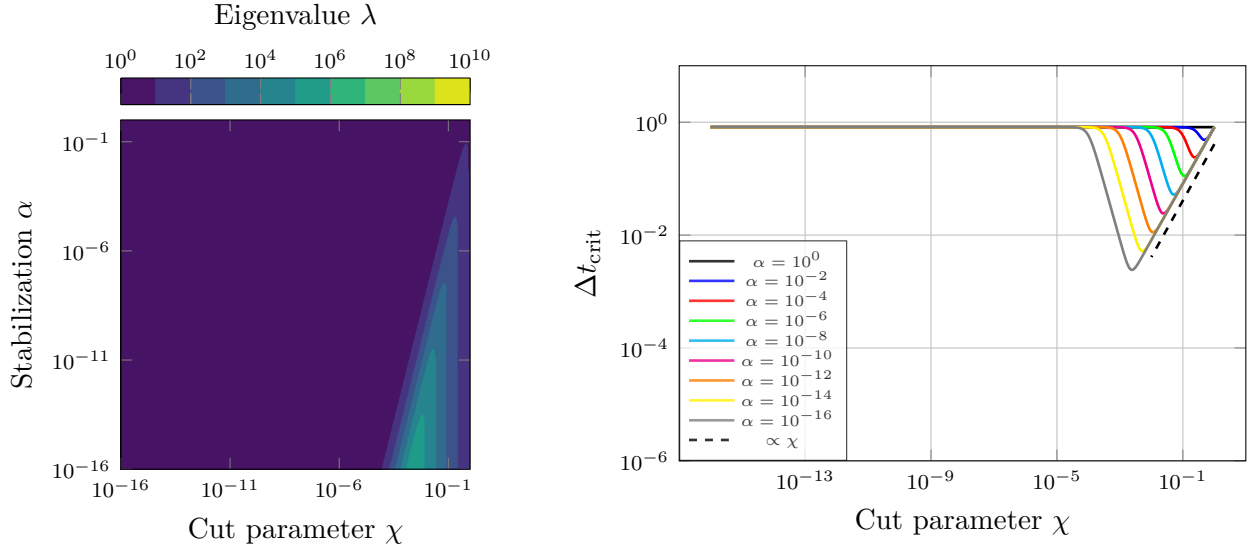


Figure 4: Eigenvalue λ (left) and corresponding critical time step size Δt_{crit} (right) of the two-dimensional system with one degree of freedom.

$\nabla N = [x_2 x_3 \ x_1 x_3 \ x_1 x_2]$. The mass and stiffness are

$$\begin{aligned} M(\chi, \alpha) &= \int_0^\chi \int_0^\chi \int_0^\chi (1 - \alpha) x_1^2 x_2^2 x_3^2 dx_1 dx_2 dx_3 + \int_0^1 \int_0^1 \int_0^2 \alpha x_1^2 x_2^2 x_3^2 dx_1 dx_2 dx_3 \\ &= \frac{1}{27} ((1 - \alpha) \chi^9 + \alpha), \end{aligned} \quad (18)$$

$$\begin{aligned} K(\chi, \alpha) &= \int_0^\chi \int_0^\chi \int_0^\chi (1 - \alpha) (x_2^2 x_3^2 + x_1^2 x_3^2 + x_1^2 x_2^2) dx_1 dx_2 dx_3 \\ &\quad + \int_0^1 \int_0^1 \int_0^1 \alpha (x_2^2 x_3^2 + x_1^2 x_3^2 + x_1^2 x_2^2) dx_1 dy_2 dz_3 \\ &= \frac{1}{3} ((1 - \alpha) \chi^7 + \alpha) \end{aligned} \quad (19)$$

and the corresponding eigenvalue is

$$\lambda(\chi, \alpha) = 9 \frac{(1 - \alpha) \chi^7 + \alpha}{(1 - \alpha) \chi^9 + \alpha}. \quad (20)$$

Accordingly, the eigenvalue and the critical time step size depending on χ and α are shown in Figure 5.

In general, when considering a d -dimensional problem, M and K are

$$M(\chi, \alpha) = \frac{1}{3^d} ((1 - \alpha) \chi^{3d} + \alpha), \quad (21)$$

$$K(\chi, \alpha) = \frac{d}{3^{d-1}} ((1 - \alpha) \chi^{3d-2} + \alpha) \quad (22)$$

where d denotes the spatial dimension of the problem. The eigenvalue then is

$$\lambda(\chi, \alpha) = 3d \frac{(1 - \alpha) \chi^{3d-2} + \alpha}{(1 - \alpha) \chi^{3d} + \alpha}. \quad (23)$$

Finally, Figure 6 shows the lower limit of the critical time step size with respect to α for the dimensions $d = 1, 2, 3, 4$, and 5 , denoted as $\Delta t_{\text{crit}, \min}$. The minimum critical time step size for a given, fixed α is defined as the minimum value of $\Delta t_{\text{crit}}(\chi, \alpha)$ when varying the cut parameter χ :

$$\Delta t_{\text{crit}, \min}(\alpha) = \min_{\chi} \Delta t_{\text{crit}}(\chi, \alpha). \quad (24)$$

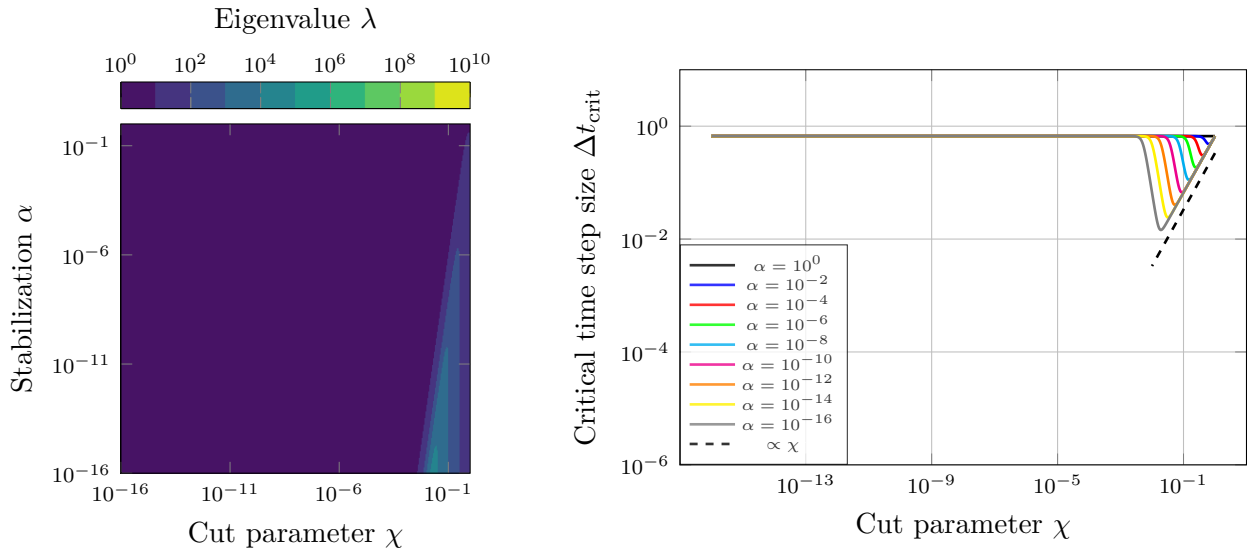


Figure 5: Eigenvalue λ (left) and corresponding critical time step size Δt_{crit} (right) of the three-dimensional system with one degree of freedom.

In the following, $\Delta t_{\text{crit},\min}(\alpha)$ is approximated by the smallest value of $\Delta t_{\text{crit}}(\chi, \alpha)$ of the sampling with respect to χ . In addition, Section 6 derives an asymptotic estimate for $\Delta t_{\text{crit},\min}(\alpha)$ as $\alpha \rightarrow 0$ that matches the scaling we obtain numerically.

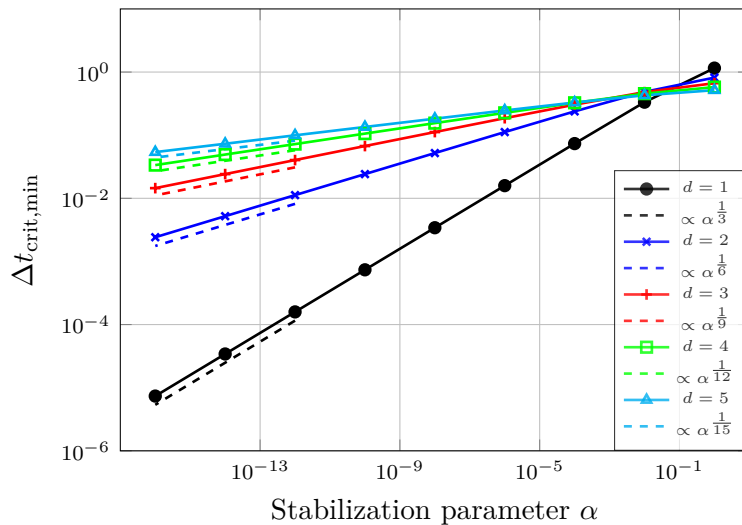


Figure 6: Minimum critical time step sizes $\Delta t_{\text{crit},\min}$ and reference lines $\propto \alpha^{\frac{1}{3d}}$ with respect to varying α for dimensions $d = 1, 2, \dots, 5$.

Discussion

The first observation is that the absence of stabilization ($\alpha = 0$) renders the eigenvalue (23) unbounded:

$$\lambda(\chi, \alpha = 0) = 3d\chi^{-2d}. \quad (25)$$

Accordingly, the critical time step is

$$\Delta t_{\text{crit}}(\chi, \alpha = 0) = \frac{2}{\sqrt{\lambda(\chi, \alpha = 0)}} = \frac{1}{\sqrt{3d}} \chi. \quad (26)$$

Regardless of the dimension d , the critical time step size decreases linearly with respect to the cut parameter χ , as shown by dashed reference lines in Figures 3 to 5. Introducing α -stabilization with $\alpha > 0$ imposes a lower limit on the mass and stiffness, and an upper limit on the eigenvalue. The eigenvalue reduces to $\lambda \rightarrow 3d$ for $\chi \rightarrow 0$. In Figures 3 to 5, we see that decreasing the cut parameter leads to a nearly linear decrease in the critical time step size until a minimum is reached which corresponds to a cut parameter $\chi \neq 0$ and depends on α . After reaching the minimum, the critical time step size starts to increase again for decreasing χ . As already seen in Figures 3 to 5, the problem of critical time step sizes becomes less severe for higher dimensional problems. We also observe that increasing the stabilization not only increases the critical time step size, but also shifts the cut parameter for which the minimum values are obtained towards higher values. In Figure 6, we see that the minimum critical time step size is proportional to $\alpha^{\frac{1}{3d}}$. Considering a three-dimensional problem and choosing $\alpha = 10^{-9}$, the critical time step size does not decrease to less than a tenth of the corresponding critical time step size of the uncut element. Finally, we observe that for $\alpha > 0$ the critical time step size of an empty element ($\chi = 0$) is equal to the critical time step size of a full element ($\chi = 1$) and independent of α :

$$\Delta t_{\text{crit}}(\chi = 0, \alpha) = \Delta t_{\text{crit}}(\chi = 1, \alpha) = \frac{1}{\sqrt{3d}}. \quad (27)$$

4 Numerical Investigations

Problem statement

The solution of wave propagation problems benefits from the spectral convergence of higher-order polynomial approximations of smooth functions. Increasing the polynomial degree p to 4 or 5 is widely applied in practice with the spectral element method [9]. The following numerical study examines how increasing the polynomial degree affects the risk of an intolerably small critical time step size by systematically varying the cut parameter χ , the stabilization parameter α , and the polynomial degree p for dimensions $d = 1, 2$, and 3. To this end, the previous example with one degree of freedom of Section 4 depicted in Figure 1 is adapted. We omit all Dirichlet boundary conditions and assume homogeneous Neumann boundary conditions on $\partial\Omega$. The number of basis functions then is $(p+1)^d$, where d is the spatial dimension of the problem and p is the polynomial degree of the univariate shape functions. This results in mass and stiffness matrices \mathbf{M} and \mathbf{K} of size $(p+1)^d \times (p+1)^d$, and the corresponding largest eigenvalue $\lambda_{\max}(\mathbf{K}, \mathbf{M})$ of the generalized eigenvalue problem. The components of the matrices are

$$M_{ij} = \int_{\Omega} (1 - \alpha) N_i(\mathbf{x}) N_j(\mathbf{x}) d\Omega + \int_{\Omega^e} \alpha N_i(\mathbf{x}) N_j(\mathbf{x}) d\Omega^e, \quad (28)$$

$$K_{ij} = \int_{\Omega} (1 - \alpha) \nabla N_i(\mathbf{x}) \cdot \nabla N_j(\mathbf{x}) d\Omega + \int_{\Omega^e} \alpha \nabla N_i(\mathbf{x}) \cdot \nabla N_j(\mathbf{x}) d\Omega^e. \quad (29)$$

The integrals in (28) and (29) are evaluated with Gauss Legendre quadrature with $p+1$ integration points per spatial direction. Thus, even with a full or uncut element, i.e. $\chi = 1$, the corresponding mass matrix is not diagonal since instead of using nodal lumping the mass matrix is integrated exactly. The SciPy function `scipy.sparse.linalg.eigsh` is used to compute the largest eigenvalue of the problem [40].

Results

For 1D, 2D, and 3D, the polynomial degree is varied between $p = 1, 2, \dots, 10$. Furthermore, three different values of stabilization $\alpha = 10^{-4}, 10^{-8}$ and 10^{-12} are examined. The cut parameter is varied in $\chi \in [10^{-8}, 10^0]$ with 161 logarithmically spaced values. The left sides of Figures 7, 8 and 9 show the critical time step sizes for 1D, 2D and 3D of all computed configurations. The three colors distinguish the different α -values, while within each color, the varying line styles encode the different polynomial degrees. Using the definition of the minimum critical time step size $\Delta t_{\text{crit}, \min}$ introduced in (24), and the corresponding critical time step size of the full element, the right sides of Figures 7,

8, and 9 show the ratio between the minimum and full critical time step size with respect to p for each α . The critical time step size of a full element, defined as

$$\Delta t_{\text{crit,full}} = \Delta t_{\text{crit}}(\chi = 1), \quad (30)$$

is independent of the stabilization parameter α . Note that $\Delta t_{\text{crit,full-c}}$ refers to the critical time step size considering an exactly integrated, consistent mass matrix of an uncut element. The critical time step size considering the diagonal mass matrix obtained by nodal lumping of a full element is denoted by $\Delta t_{\text{crit,full-l}}$.

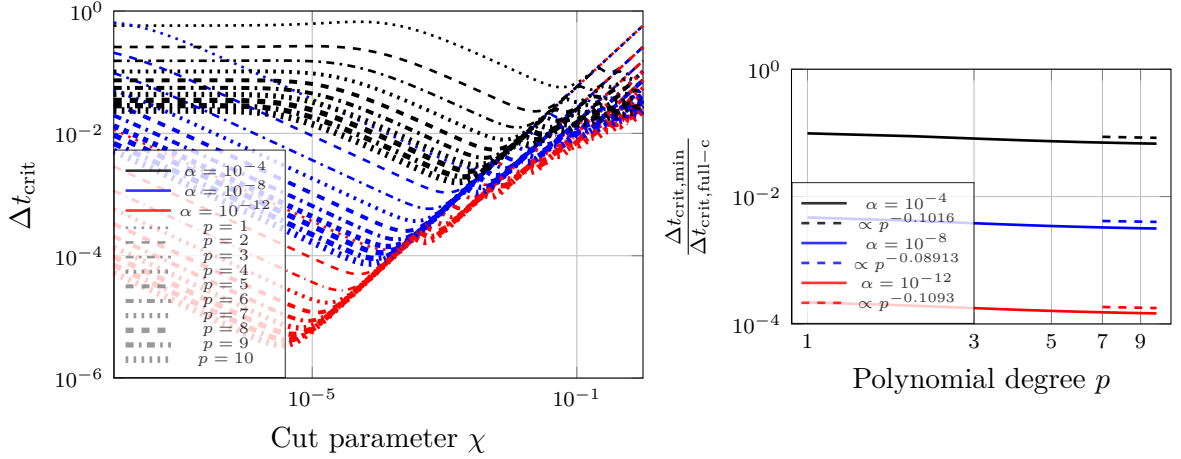


Figure 7: Critical time step size Δt_{crit} (left) and minimum critical time step size ratio $\frac{\Delta t_{\text{crit,min}}}{\Delta t_{\text{crit,full-c}}}$ (right) for $p = 1, 2, \dots, 10$ in 1D.

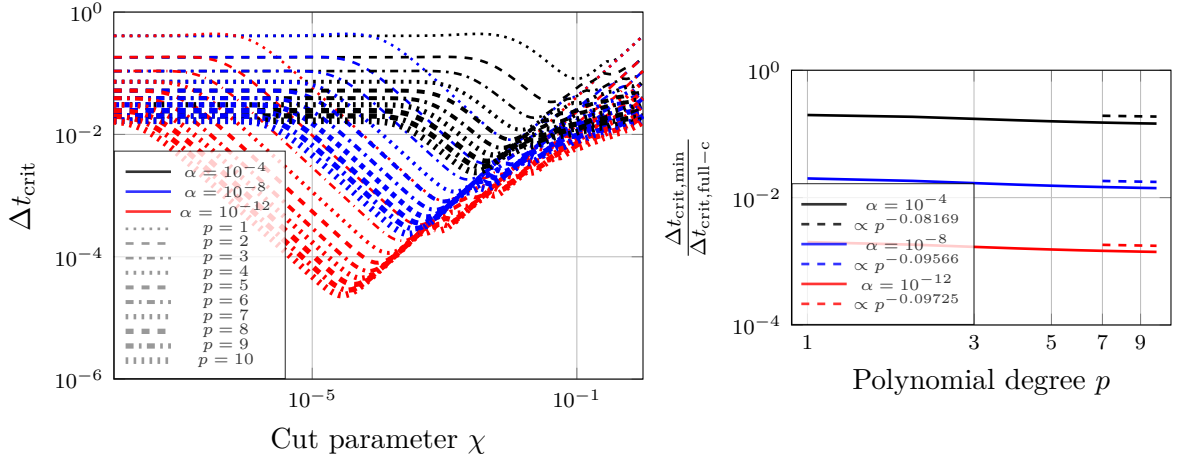


Figure 8: Critical time step size Δt_{crit} (left) and minimum critical time step size ratio $\frac{\Delta t_{\text{crit,min}}}{\Delta t_{\text{crit,full-c}}}$ (right) for $p = 1, 2, \dots, 10$ in 2D.

Discussion

Compared to the example with one unknown in the previous section, the decrease of the critical time step size Δt_{crit} , follows a more complicated relation in the current example with higher polynomial degrees. Multiple minima occur when increasing p . Overall, the critical time step size still decreases until a global minimum is reached, and increases again afterwards. Moreover, it also holds that the critical time step size is unbounded without stabilization, and that the minimum critical time step size becomes less detrimental with increasing dimension. Higher stabilization parameters lead to

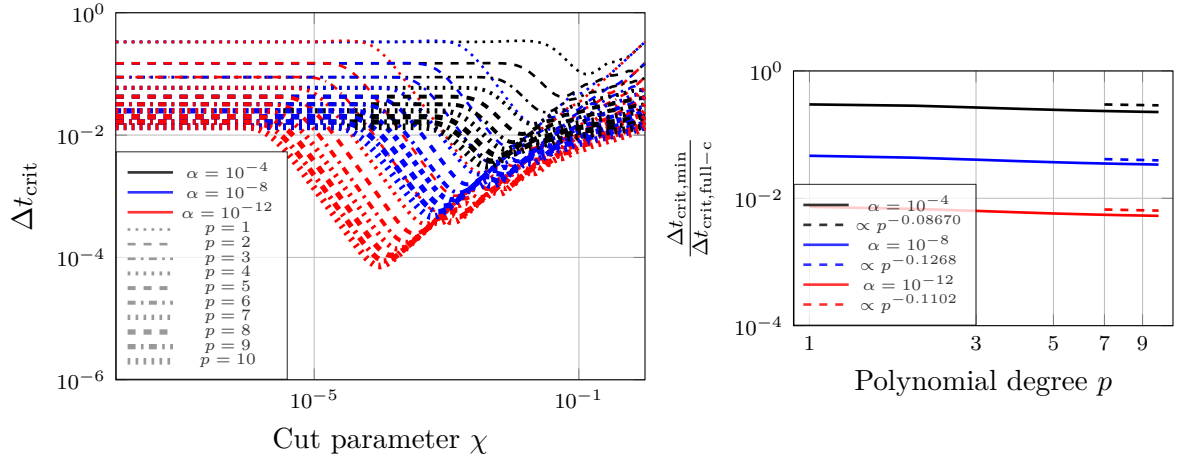


Figure 9: Critical time step size Δt_{crit} (left) and minimum critical time step size ratio $\frac{\Delta t_{\text{crit},\text{min}}}{\Delta t_{\text{crit},\text{full-c}}}$ (right) for $p = 1, 2, \dots, 10$ in 3D.

larger minimum critical time step sizes and increasing cut parameter values at which the minimum critical time step size occurs, independent of the polynomial degree p . In addition, the right sides of Figures 7 to 9 show that the ratio of the minimum to the full critical time step size only depends weakly on the polynomial degree p . This was verified by a study with increasing polynomial degrees until $p = 20$, where the slope of the curve further decreased. In other words, the severity of reduced critical time step sizes regarding explicit time integration introduced by cut elements does not increase significantly with increasing polynomial degrees.

5 A modified FCM-CFL condition

Minimum critical time step size estimate

To develop a generally applicable estimate for the lower bound of the critical time step size in the form of a modified Courant–Friedrichs–Lewy (CFL) condition [11] tailored to FCM, we further investigate the example of the previous section (again without Dirichlet boundary conditions). For each polynomial degree between $p = 1$ and $p = 10$ we now choose nine logarithmically-spaced α -values within the interval $[10^{-16}, 10^0]$. Figure 10 shows the ratio between the minimum and full (uncut) critical time step sizes $\Delta t_{\text{crit},\text{min}}$ and $\Delta t_{\text{crit},\text{full-c}}$ with respect to α for different p and dimensions $d = 1, 2$, and 3. All curves are proportional to and above the reference curves, which are $\alpha^{\frac{1}{3}}$ in 1D, $\alpha^{\frac{1}{4}}$ in 2D, and $\alpha^{\frac{1}{5}}$ in 3D. We conclude empirically that

$$\Delta t_{\text{crit},\text{min}} \geq \alpha^{\frac{1}{d+2}} \Delta t_{\text{crit},\text{full-c}} \quad (31)$$

for dimensions $d = 1, 2$, and 3, where $t_{\text{crit},\text{full-c}}$ is the critical time step size of the full element with a consistently integrated mass matrix for the given polynomial degrees (e.g. using $p+1$ Gauss-Legendre points per direction). Interestingly, the scaling for higher dimensions is different to our results from Section 3. We assume, that this difference is due to the way we define Dirichlet boundary conditions to obtain a single-DOF system.

Equation (31) provides a lower limit to how much the critical time step size may decrease in the worst case for a given α -stabilization, i.e., in the presence of the most unfavorable cut configuration. This estimate allows us to derive a CFL-condition for FCM in terms of the underlying spatial and temporal (base-)discretization. In the general case, the CFL-condition limits the time step size as follows:

$$\Delta t \leq C_{\text{CFL}}(p) \frac{h}{c}, \quad (32)$$

where h is the element size, c the wave speed, and $0 < C_{\text{CFL}} \leq 1$ a constant that depends on the dimension of the problem, the time integration scheme, and the spatial discretization method

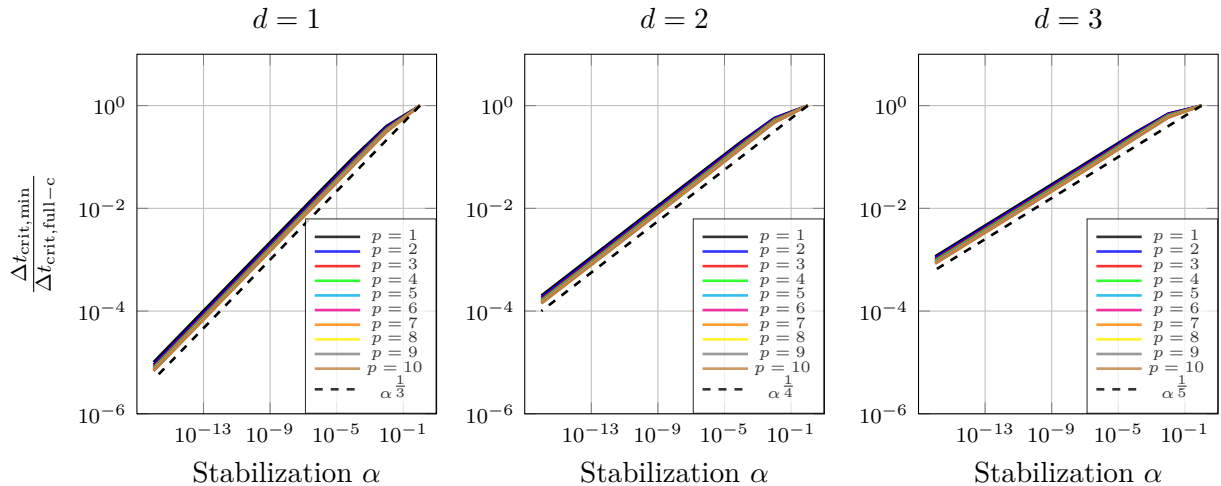


Figure 10: Ratio between minimum and full critical time step size when varying α for polynomial degrees $p = 1, 2, \dots, 10$ and dimensions $d = 1, 2, 3$. The dashed lines are the reference curves $\alpha^{\frac{1}{d+2}}$.

(particularly its polynomial degree) [9]. In our case, C_{CFL} is chosen for an SEM discretization of polynomial degree p , integrated in time using the CDM. By combining (32) and (31), we arrive at the modified CFL condition

$$\Delta t \leq \alpha^{\frac{1}{d+2}} C_{\text{CFL}}(p) \frac{h}{c}. \quad (33)$$

The estimate introduced by (33) provides a lower limit for choosing an appropriate time step size when using α -stabilization. While $C_{\text{CFL}}(p)$ in (32) is defined for the lumped mass matrix in an SCM-context, the constant in (33) instead relates to the consistent mass matrix.

Perforated plate study

In this section, we verify (31) and (33) on a perforated plate with dimensions 9×3 , as Figure 11 shows. The plate features three columns of circular holes with equal radii $r_i = r = \frac{3}{13}$ and equal horizontal and vertical spacing of $3 \cdot r = \frac{9}{13}$. The middle column is aligned with the horizontal center of the plate. We choose $\rho = c = 1$ and reflecting (homogeneous Neumann) boundary conditions on $\partial\Omega$. We do not define an excitation since the computation of the critical time step size does not require one. The SCM-discretization of the plate uses a regular grid of 45×15 elements, stabilized with $\alpha = 10^{-4}$, resulting in an element size of $h = 0.2$. We integrate uncut cells with $p + 1$ GLL points per spatial direction to obtain a diagonal mass matrix and $p + 1$ Gauss-Legendre (GL) points per direction for the stiffness matrix. The quadrature of cut elements refines a quadtree k times towards the domain boundary and distributes $p + 1$ GL points per direction on its leaves to integrate both element mass and stiffness matrices.

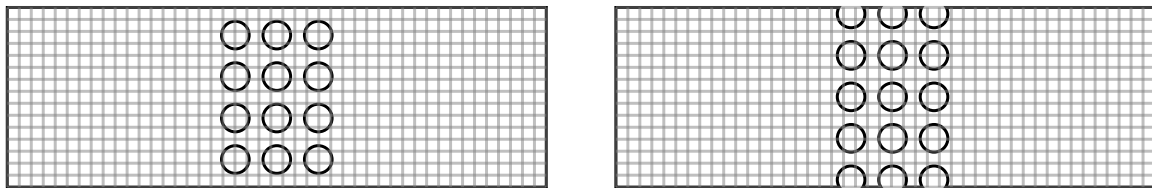


Figure 11: Perforated plate with computational mesh: Configuration #1 with $\Delta x = 0.0$ and $\Delta y = 0.0$ (left); Configuration #428 with $\Delta x = 0.12$ and $\Delta y = 0.35385$ (right).

Using this setup, we now study the critical time step size while slightly shifting the circle positions

in the x - and y -directions up to maximum distances of $\Delta x_{\max} = h = 0.2$ and $\Delta y_{\max} = 3r = \frac{9}{13}$. We evaluate different position shifts on a linearly spaced grid with 15 evaluation points in x and 50 points in y , resulting in a total of 750 configurations. During the translation in the y -direction, the top row of circles crosses the upper boundary, while new circles enter below. Figures 12 to 15 show five different types of critical time step sizes for all configurations and polynomial degrees $p = 2, 3, 4$, and 5. The results on the left were obtained with a quadtree depth of $k = p + 1$ and on the right with $k = p + 2$. The blue lines ($\Delta t_{\text{crit,full-l}}$) show the critical time step sizes of an uncut element obtained with nodal lumping for the mass matrix, and the green lines ($\Delta t_{\text{crit,full-c}}$) show the critical time step sizes of an uncut consistent element when the mass matrix is not under integrated. Both values are independent of the geometric configuration. The dashed red lines ($\Delta t_{\text{crit,cfl,fc}}$) estimate the the minimum critical time step size according to (31). Since in this study, we have $d = 2$ and $\alpha = 10^{-4}$, our estimate evaluates to

$$\Delta t_{\text{crit,cfl,fc}} = \left(10^{-4}\right)^{\frac{1}{4}} \Delta t_{\text{crit,full-c}} = \frac{1}{10} \Delta t_{\text{crit,full-c}}. \quad (34)$$

The black dots ($\Delta t_{\text{crit,element}}$) then show for all configurations the smallest critical time step size of all elements computed individually, while the purple dots ($\Delta t_{\text{crit,global}}$) show for each configuration the critical time step sizes of the global system.

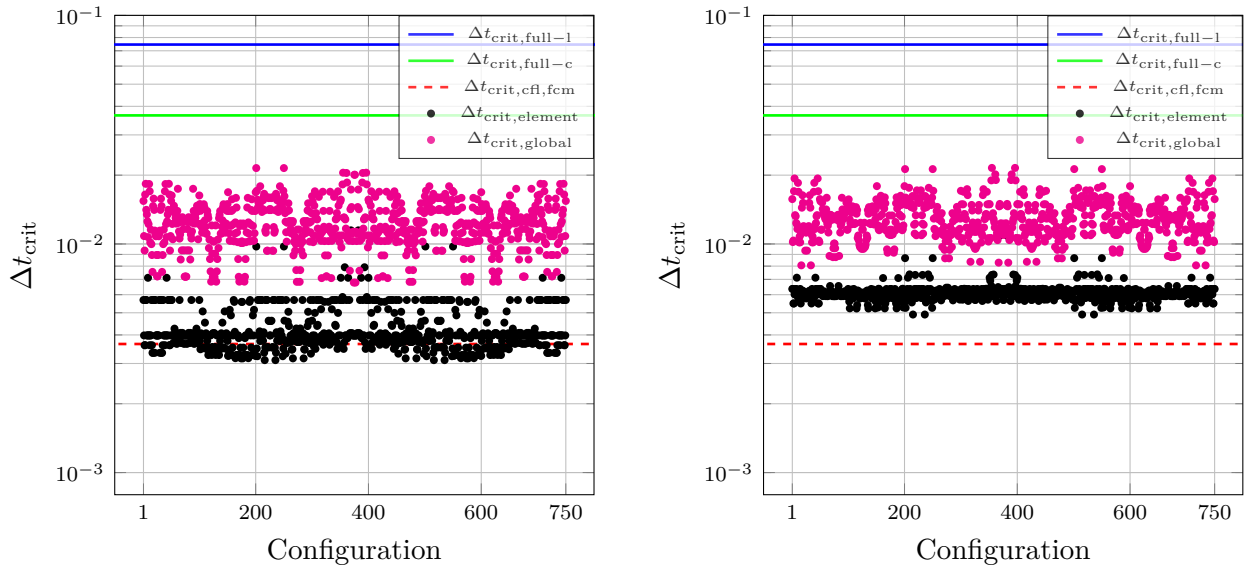


Figure 12: Critical time step sizes for $p = 2$: $k = 3$ (left) and $k = 4$ (right).

The first observation is that an inaccurate quadrature of cut elements can severely impact the critical time step size, as the left side of Figure 12 shows. Here, three quadtree levels are insufficient to integrate the second-order elements and thus our CFL condition is violated at the element level for some configurations, visible by several black dots below the dashed red line. Increasing the quadtree depth to four levels ($p + 2$) increases all critical time step sizes above the level of our adjusted CFL condition. This stability degradation is not observed for higher polynomial degrees, indicating that increasing k linearly with p may not balance the effect of the quadrature error appropriately during p -refinement. Another observation is that the global critical time steps are larger than the critical time step sizes computed element-wise, since the connectivity of the basis functions between elements mitigates some of the negative effect of badly cut elements. For this reason, the proposed equation also serves as a lower limit for an estimating the global critical time step size, although it is very conservative.

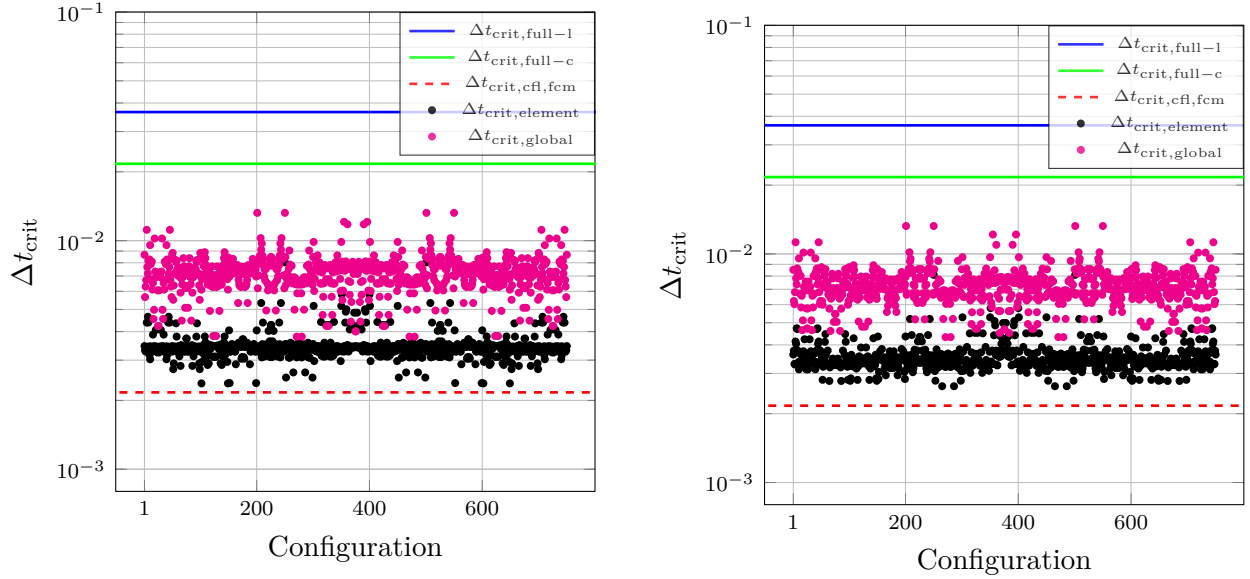


Figure 13: Critical time step sizes for $p = 3$: $k = 4$ (left) and $k = 5$ (right).

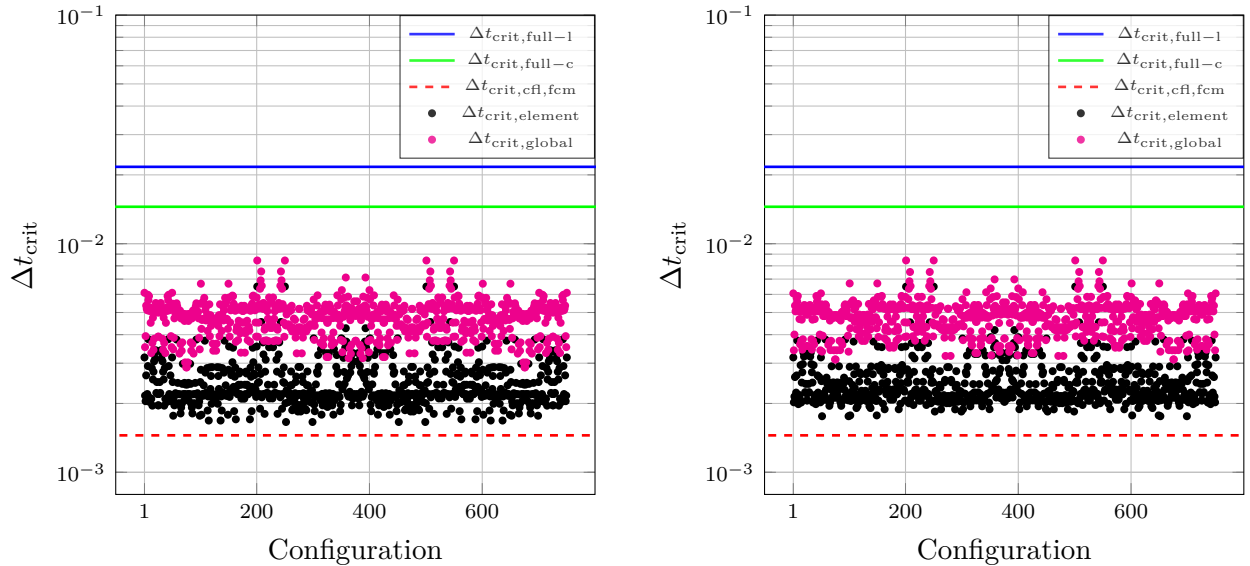


Figure 14: Critical time step sizes for $p = 4$: $k = 5$ (left) and $k = 6$ (right).

6 Conclusion

We investigate the challenge of restrictive critical time step sizes in explicit time integration arising from badly cut elements in immersed boundary methods. Applying the finite cell method, the addition of non-zero α -values in the fictitious domain prevents the mass and stiffness of the discretized system from reaching zero, thereby imposing a lower limit on the critical time step size. We first analytically study a linearly-interpolated single-element example, where we investigate the behavior of the critical time step size with respect to the cut position, the stabilization value, and the spatial dimension. We show that the critical time step size does not continue to decrease for arbitrarily small cut ratios, but reaches a minimum for finite values of α . This minimum critical time step size decreases with $\Delta_{\text{crit},\text{min}} \propto \alpha^{\frac{1}{3d}}$. The problem of infeasibly small critical time step sizes becomes less detrimental for higher dimensions, making α -stabilization a viable option in 2D and 3D. We then

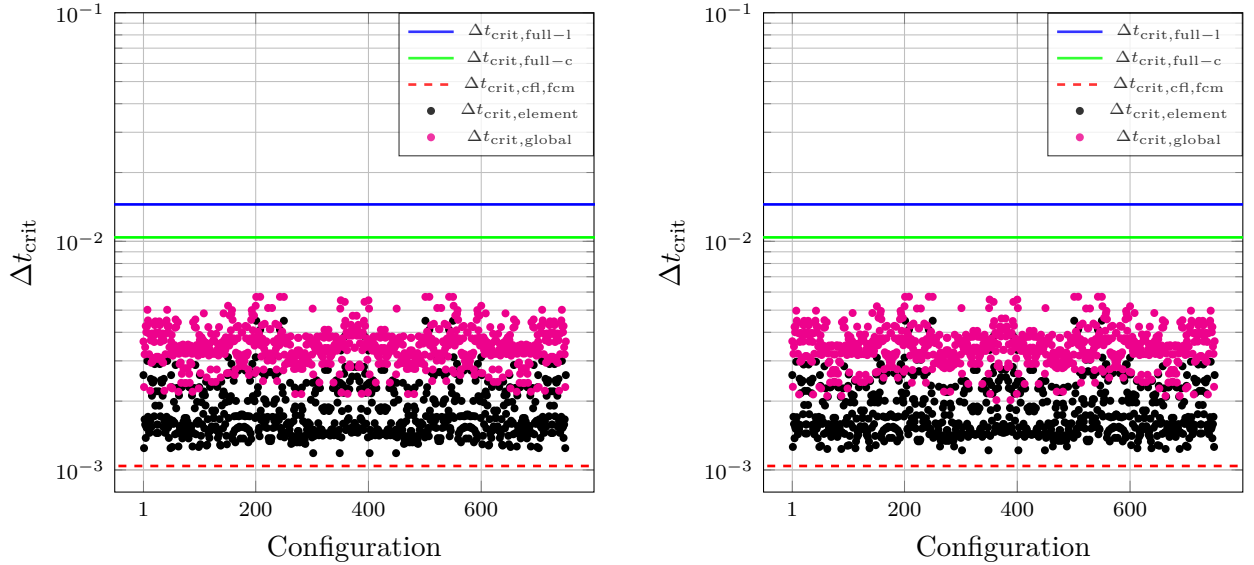


Figure 15: Critical time step sizes for $p = 5$: $k = 6$ (left) and $k = 7$ (right).

extend our analysis to high-order polynomials, where we numerically study the dependence of the critical time step size on the polynomial degree. Here, α -stabilization again imposes a lower limit on the critical time step size and this limit becomes less severe in higher dimensions. We show that the adverse effects of cut elements only weakly depend on the polynomial degree. Based on these results, we propose an estimate of the minimum critical time step size with respect to the dimension and the stabilization parameter. Our results imply that the critical time step size of a cut element decreases by a factor of $\alpha^{\frac{1}{d+2}}$ in the most unfavorable cut configuration. From this estimate, we derive a CFL condition for the finite cell method that multiplies the critical time step of the underlying base discretization by $\alpha^{\frac{1}{d+2}}$. The validity of this formula is demonstrated on a two-dimensional perforated plate with different cut configurations, while also highlighting the influence of the quadrature error on the stability.

For choosing α in practice, one must not only relate it to Δt_{crit} , but also to a measure of the consistency error. In this context, we want to mention the analysis provided by [38], which found that the finite cell method introduces an error in the energy norm proportional to $\sqrt{\alpha}$ for Laplace and Helmholtz problems. We also expect that for explicit dynamics, a relatively high stabilization, such as $\alpha = 10^{-4}$, retains sufficient accuracy for many engineering applications while permitting moderate minimum critical time step sizes in 2D and 3D.

Asymptotic minimum critical time step size of the single-DOF system

To find the largest eigenvalue for our single DOF system, i.e., maximize (23) for a given α , we require the partial derivative with respect to the cut position to vanish:

$$\frac{\partial \lambda}{\partial \chi} = \frac{3\chi^{3d-3}d(\alpha-1)(3\alpha\chi^2d - 2\alpha\chi^{3d} - 3\alpha d + 2\alpha + 2\chi^{3d})}{(-\alpha\chi^{3d} + \alpha + \chi^{3d})^2} = 0.$$

For the relevant parameter range, this expression simplifies to

$$3\alpha\chi^2d - 2\alpha\chi^{3d} - 3\alpha d + 2\alpha + 2\chi^{3d} = 0$$

or

$$\alpha(3\chi^2d - 2\chi^{3d} - 3d + 2) + 2\chi^{3d} = 0.$$

It is clear that when asymptotically reducing $\alpha \rightarrow 0$, also χ must approach zero. Since in this case the term multiplying α converges to $-3d + 2$, we know that the cut position maximizing (23) asymptotically approaches

$$2\chi^{3d} = \alpha(3d - 2) \quad \implies \quad \chi = \left(\alpha \frac{3d - 2}{2} \right)^{\frac{1}{3d}}.$$

Substituting this result into (23) yields the following asymptotic estimate for $\alpha \rightarrow 0$

$$\begin{aligned} \lambda_{\max} &\sim 3d \frac{(1 - \alpha) \left(\alpha \frac{3d-2}{2} \right)^{\frac{3d-2}{3d}} + \alpha}{(1 - \alpha) \left(\alpha \frac{3d-2}{2} \right)^{\frac{3d}{3d}} + \alpha} = 3d \frac{(1 - \alpha) \left(\frac{3d-2}{2} \right)^{1-\frac{2}{3d}} \alpha^{1-\frac{2}{3d}} + \alpha}{\frac{3d}{2}\alpha - \frac{3d-2}{2}\alpha^2} \\ &\sim 3d \frac{\left(\frac{3d-2}{2} \right)^{1-\frac{2}{3d}} \alpha^{1-\frac{2}{3d}}}{\frac{3d}{2}\alpha} \\ &\sim C_\lambda(d) \alpha^{-\frac{2}{3d}}, \end{aligned}$$

with

$$C_\lambda(d) = 2 \left(\frac{3d - 2}{2} \right)^{1-\frac{2}{3d}}.$$

Using (8), we obtain the minimum time step size for $\alpha \rightarrow 0$:

$$\Delta t_{\text{crit, min}} \sim \frac{2}{\sqrt{C_\lambda(d)}} \alpha^{\frac{1}{3d}}.$$

Acknowledgements

We gratefully acknowledge the Deutsche Forschungsgemeinschaft (DFG, German Research Foundation) for their support through the grants KO 4570/1-2 and RA 624/29-2 (both grant number 438252876) as well as DU 405/20-1 (grant number 503865803). We would also like to thank Alexander Düster, Stefan Kollmannsber, and Ernst Rank for many fruitful discussions on this topic that inspired this study.

References

- [1] J. Virieux and S. Operto, “An overview of full-waveform inversion in exploration geophysics,” *GEOPHYSICS*, vol. 74, no. 6, pp. WCC1–WCC26, 2009.
- [2] A. Fichtner, *Full Seismic Waveform Modelling and Inversion*. Advances in Geophysical and Environmental Mechanics and Mathematics, Springer Berlin Heidelberg, 2011.
- [3] J. Gu and Y. Jing, “Modeling of wave propagation for medical ultrasound: a review,” *IEEE Transactions on Ultrasonics, Ferroelectrics, and Frequency Control*, vol. 62, no. 11, pp. 1979–1992, 2015.
- [4] C. Willberg, S. Duczek, J. M. Vivar-Perez, and Z. A. B. Ahmad, “Simulation Methods for Guided Wave-Based Structural Health Monitoring: A Review,” *Applied Mechanics Reviews*, vol. 67, p. 010803, 01 2015.
- [5] H. Chen, M. Zhou, S. Gan, X. Nie, B. Xu, and Y. Mo, “Review of wave method-based non-destructive testing for steel-concrete composite structures: Multiscale simulation and multi-physics coupling analysis,” *Construction and Building Materials*, vol. 302, p. 123832, 2021.
- [6] H. Igel, *Computational Seismology: A Practical Introduction*. Oxford University Press, 2017.

- [7] D. Komatitsch and J. Tromp, “Introduction to the spectral element method for three-dimensional seismic wave propagation,” *Geophysical Journal International*, vol. 139, no. 3, pp. 806–822, 1999.
- [8] D. Komatitsch and J. Tromp, “Spectral-element simulations of global seismic wave propagation – i. validation,” *Geophysical Journal International*, vol. 149, pp. 390–412, 05 2002.
- [9] A. Ferroni, P. F. Antonietti, I. Mazzieri, and A. Quarteroni, “Dispersion-dissipation analysis of 3-D continuous and discontinuous spectral element methods for the elastodynamics equation,” *Geophysical Journal International*, vol. 211, pp. 1554–1574, 09 2017.
- [10] M. Afanasiev, C. Boehm, M. van Driel, L. Krischer, M. Rietmann, D. A. May, M. G. Knepley, and A. Fichtner, “Modular and flexible spectral-element waveform modelling in two and three dimensions,” *Geophysical Journal International*, vol. 216, pp. 1675–1692, 11 2018.
- [11] H. Lewy, K. Friedrichs, and R. Courant, “Über die partiellen differenzgleichungen der mathematischen physik,” *Mathematische Annalen*, vol. 100, pp. 32–74, 1928.
- [12] M. Ainsworth, “Dispersive and dissipative behaviour of high order discontinuous galerkin finite element methods,” *J. Comput. Phys.*, vol. 198, no. 1, pp. 106–130, 2004.
- [13] L. Radtke, D. Müller, and A. Düster, “Optimally blended spectral elements in structural dynamics: Selective integration and mesh distortion,” *International Journal of Computational Methods*, vol. 18, no. 10, p. 2150042, 2021.
- [14] F. de Prenter, C. V. Verhoosel, E. H. van Brummelen, M. G. Larson, and S. Badia, “Stability and conditioning of immersed finite element methods: Analysis and remedies,” *Archives of Computational Methods in Engineering*, vol. 30, 2023.
- [15] L. Radtke, M. Torre, T. J. Hughes, A. Düster, G. Sangalli, and A. Reali, “An analysis of high order fem and iga for explicit dynamics: Mass lumping and immersed boundaries,” *International Journal for Numerical Methods in Engineering*, vol. 125, no. 16, p. e7499, 2024.
- [16] A. Düster, E. Rank, and B. Szabó, “The p-Version of the Finite Element and Finite Cell Methods,” in *Encyclopedia of Computational Mechanics Second Edition* (E. Stein, R. Borst, and T. Hughes, eds.), pp. 1–35, 2017.
- [17] T. Bürchner, P. Kopp, S. Kollmannsberger, and E. Rank, “Immersed boundary parametrizations for full waveform inversion,” *Computer Methods in Applied Mechanics and Engineering*, vol. 406, p. 115893, 2023.
- [18] D. Schillinger, L. Dedè, M. A. Scott, J. A. Evans, M. J. Borden, E. Rank, and T. J. Hughes, “An isogeometric design-through-analysis methodology based on adaptive hierarchical refinement of nurbs, immersed boundary methods, and t-spline cad surfaces,” *Computer Methods in Applied Mechanics and Engineering*, vol. 249-252, pp. 116–150, 2012. Higher Order Finite Element and Isogeometric Methods.
- [19] M. Meßmer, T. Teschemacher, L. F. Leidinger, R. Wüchner, and K.-U. Bletzinger, “Efficient cad-integrated isogeometric analysis of trimmed solids,” *Computer Methods in Applied Mechanics and Engineering*, vol. 400, p. 115584, 2022.
- [20] S. K. Stoter, S. C. Divi, E. H. van Brummelen, M. G. Larson, F. de Prenter, and C. V. Verhoosel, “Critical time-step size analysis and mass scaling by ghost-penalty for immersogeometric explicit dynamics,” *Computer Methods in Applied Mechanics and Engineering*, vol. 412, p. 116074, 2023.
- [21] E. Burman, S. Claus, P. Hansbo, M. G. Larson, and A. Massing, “Cutfem: Discretizing geometry and partial differential equations,” *International Journal for Numerical Methods in Engineering*, vol. 104, no. 7, pp. 472–501, 2015.
- [22] S. Sticker, G. Ludvigsson, and G. Kreiss, “High-order cut finite elements for the elastic wave equation,” *Advances in Computational Mathematics*, vol. 46, 05 2020.
- [23] S. Badia, F. Verdugo, and A. F. Martín, “The aggregated unfitted finite element method for elliptic problems,” *Computer Methods in Applied Mechanics and Engineering*, vol. 336, pp. 533–553, 2018.
- [24] E. Burman, P. Hansbo, and M. G. Larson, “Explicit time stepping for the wave equation us-

- ing cutfem with discrete extension,” *SIAM Journal on Scientific Computing*, vol. 44, no. 3, pp. A1254–A1289, 2022.
- [25] E. Nadal, J. J. Ródenas, J. Albelda, M. Tur, J. E. Tarancón, and F. J. Fuenmayor, “Efficient Finite Element Methodology Based on Cartesian Grids: Application to Structural Shape Optimization,” *Abstract and Applied Analysis*, vol. 2013, no. SI51, pp. 1 – 19, 2013.
- [26] A. Main and G. Scovazzi, “The shifted boundary method for embedded domain computations. part i: Poisson and stokes problems,” *Journal of Computational Physics*, vol. 372, pp. 972–995, 2018.
- [27] T. Song, A. Main, G. Scovazzi, and M. Ricchiuto, “The shifted boundary method for hyperbolic systems: Embedded domain computations of linear waves and shallow water flows,” *Journal of Computational Physics*, vol. 369, pp. 45–79, 2018.
- [28] S. Eisenträger, L. Radtke, W. Garhuom, S. Löhnert, A. Düster, D. Juhre, and D. Schillinger, “An eigenvalue stabilization technique for immersed boundary finite element methods in explicit dynamics,” *Computers & Mathematics with Applications*, vol. 166, pp. 129–168, 2024.
- [29] S. Schoeder, S. Sticker, G. Kreiss, and M. Kronbichler, “High-order cut discontinuous galerkin methods with local time stepping for acoustics,” *International Journal for Numerical Methods in Engineering*, vol. 121, no. 13, pp. 2979–3003, 2020.
- [30] S. Nicoli, K. Agathos, and E. Chatzi, “Moment fitted cut spectral elements for explicit analysis of guided wave propagation,” *Computer Methods in Applied Mechanics and Engineering*, vol. 398, p. 115140, 2022.
- [31] S. May and M. Berger, “An explicit implicit scheme for cut cells in embedded boundary meshes,” *Journal of Scientific Computing*, vol. 71, no. 3, pp. 919–943, 2017.
- [32] C. Faßbender, T. Burchner, P. Kopp, E. Rank, and S. Kollmannsberger, “Implicit-explicit time integration for the immersed wave equation,” *Computers & Mathematics with Applications*, vol. 163, pp. 1–13, 2024.
- [33] S. Nicoli, K. Agathos, and E. Chatzi, “On variationally consistent versus heuristic mass formulations in cut and extended finite element methods,” *Computer Methods in Applied Mechanics and Engineering*, vol. 432, p. 117393, 2024.
- [34] A. M. Carson, J. W. Banks, W. D. Henshaw, and D. W. Schwendeman, “High-order accurate implicit-explicit time-stepping schemes for wave equations on overset grids,” *Journal of Computational Physics*, vol. 520, p. 113513, 2025.
- [35] T. Burchner, P. Kopp, L. Radtke, S. Kollmannsberger, E. Rank, and A. Düster, “On the efficiency of explicit and semi-explicit immersed boundary finite element methods for wave propagation problems,” *under review in Advances in Computational Science and Engineering, WCCM 2024 Special issue*, 2025.
- [36] S. Duczek, M. Joulaiian, A. Düster, and U. Gabbert, “Numerical analysis of lamb waves using the finite and spectral cell methods,” *International Journal for Numerical Methods in Engineering*, vol. 99, no. 1, pp. 26–53, 2014.
- [37] M. Joulaiian, S. Duczek, U. Gabbert, and A. Düster, “Finite and spectral cell method for wave propagation in heterogeneous materials,” *Computational Mechanics*, vol. 54, 2014.
- [38] M. Dauge, A. Düster, and E. Rank, “Theoretical and numerical investigation of the finite cell method,” *Journal of Scientific Computing*, vol. 65, p. 1039–1064, 2015.
- [39] T. J. Hughes, *The finite element method: linear static and dynamic finite element analysis*. Courier Corporation, 2012.
- [40] P. Virtanen, R. Gommers, T. E. Oliphant, M. Haberland, T. Reddy, D. Cournapeau, E. Burovski, P. Peterson, W. Weckesser, J. Bright, S. J. van der Walt, M. Brett, J. Wilson, K. J. Millman, N. Mayorov, A. R. J. Nelson, E. Jones, R. Kern, E. Larson, C. J. Carey, Í. Polat, Y. Feng, E. W. Moore, J. VanderPlas, D. Laxalde, J. Perktold, R. Cimrman, I. Henriksen, E. A. Quintero, C. R. Harris, A. M. Archibald, A. H. Ribeiro, F. Pedregosa, P. van Mulbregt, and SciPy 1.0 Contributors, “SciPy 1.0: Fundamental Algorithms for Scientific Computing in Python,” *Nature Methods*, vol. 17, pp. 261–272, 2020.